Astronomy & Astrophysics manuscript no. main
February 9, 2022

Heating of the solar chromosphere through current dissipation

J. M. da Silva Santos[1,2], S. Danilovic[1], J. Leenaarts[1], J. de la Cruz Rodríguez[1], X. Zhu[3,4], S. M. White[5], G. J. M. Vissers[1], and M. Rempel[6]

[1] Institute for Solar Physics, Department of Astronomy, Stockholm University, AlbaNova University Centre, SE-106 91 Stockholm, Sweden
[2] National Solar Observatory, University of Colorado, 3665 Discovery Drive, Boulder, CO 80303, USA
e-mail: `jdasilvasantos@nso.edu`
[3] Key Laboratory of Solar Activity, National Astronomical Observatories, Chinese Academy of Sciences, Beijing 100012, China
[4] Max-Planck-Institut für Sonnensystemforschung, Justus-von-Liebig-Weg 3, 37077 Göttingen, Germany
[5] Space Vehicles Directorate, Air Force Research Laboratory, Albuquerque, NM, USA
[6] High Altitude Observatory, National Center for Atmospheric Research, 80307, Boulder, CO, USA

ABSTRACT

Context. The solar chromosphere is heated to temperatures higher than predicted by radiative equilibrium. This excess heating is larger in active regions where the magnetic field is stronger.

Aims. We aim to investigate the magnetic topology associated to an area of enhanced millimeter (mm) brightness temperatures in a solar active region mapped by the Atacama Large Millimeter/submillimeter Array (ALMA) using spectropolarimetric coobservations with the 1-m Swedish Solar Telescope (SST).

Methods. We use Milne-Eddington inversions, nonlocal thermodynamic equilibrium (non-LTE) inversions, and a magnetohydrostatic extrapolation to obtain constraints on the three-dimensional stratification of temperature, magnetic field, and radiative energy losses. We compare the observations to a snapshot of a magnetohydrodynamics simulation and investigate the formation of the thermal continuum at 3 mm using contribution functions.

Results. We find enhanced heating rates in the upper chromosphere of up to $\sim$5 kW m^{-2} where small-scale emerging loops interact with the overlying magnetic canopy leading to current sheets as shown by the magnetic field extrapolation. Our estimates are about a factor of two higher than canonical values, but they are limited by the ALMA spatial resolution ($\sim 1.2''$). Band 3 brightness temperatures reach about $\sim 10^4$ K in the region, and the transverse magnetic field strength inferred from the non-LTE inversions is of the order of ~ 500 G in the chromosphere.

Conclusions. We quantitatively reproduce many of the observed features including the integrated radiative losses in our numerical simulation, and we conclude that the heating is caused by dissipation in current sheets. However, the simulation shows a complex stratification in the flux emergence region where distinct layers may contribute significantly to the emission in the mm continuum.

Key words. Sun: atmosphere – Sun: chromosphere – Sun: magnetic fields – Sun: radio radiation – Sun: activity

1. Introduction

The heating of the solar chromosphere and corona is mediated by magnetic fields, which guide Poynting flux generated by plasma motions in the convection zone into the outer atmosphere and provide a means to convert the transported energy into heat. The conversion mechanisms can be broadly divided into dissipation of wave energy (e.g., Van Doorsselaere et al. 2020) and dissipation of electric currents induced by the slow evolution of the magnetic field (e.g., Parker 1988), but their relative contribution to the energy balance is still unclear. In the quiet-Sun (QS) chromosphere, heating by acoustic waves may (Abbasvand et al. 2020) or may not (Molnar et al. 2021) be the dominant process, but active-regions (ARs) definitely require other energy sources.

Research has focused mostly on the corona (e.g., McIntosh et al. 2011; Cirtain et al. 2013; Hansteen et al. 2015; Klimchuk 2015) but much less on the chromosphere, which requires more sophisticated models that only recently became sufficiently realistic to allow for quantitative comparisons with observations (Carlsson et al. 2019). Furthermore, it is not trivial to interpret spectral diagnostics formed under optically thick, nonlocal thermodynamic equilibrium (non-LTE) conditions, such as the resonance lines of Mg II and Ca II, which require detailed three-dimensional (3-D) radiative transfer calculations including partial frequency redistribution for full accuracy (see review by de la Cruz Rodríguez & van Noort 2017).

However, energy losses are much larger in the chromosphere than in the corona: canonical estimates of average (total) losses for QS and AR are 4 kW m^{-2} and 20 kW m^{-2} for the chromosphere but only 0.3 kW m^{-2} and $<$ 10 kW m^{-2}, respectively, for the corona (Withbroe & Noyes 1977). In the era of high-resolution solar physics the focus should shift to obtaining new detailed models that reproduce the observed fine structure rather than averaged observables (Carlsson et al. 2019). Yet studies quantifying spatially and temporally resolved energy losses are scarce. Recent estimates with a time resolution of 30 s and a spatial resolution of $\sim$100 km indicate losses that can locally be as high as 160 kW m^{-2} in the chromosphere (Díaz Baso et al. 2021). This was attributed to magnetic reconnection but no attempt was made at reconciling simulations with observations.

It is well-established that radiative cooling is stronger in regions where the magnetic field is more concentrated, but this relationship is not linear (e.g., Schrijver 1987; Harvey & White 1999; Barczynski et al. 2018). Low resolution ($\gtrsim 10''$) observations in the millimeter range show brightness enhancements associated with network and ARs (e.g., Lindsey & Jefferies 1991; Loukitcheva et al. 2009), while high-resolution (∼ 0.1″) optical observations show that the Ca ii K brightness in ARs is dominated by an extended component that is associated with more space-filling, horizontal magnetic fields (Leenaarts et al. 2018).

Dissipation of electric currents induced by the magnetic field is a prime candidate for this heating, but determining the electric current vector in the chromosphere is notoriously challenging and it has only been reported in sunspots using Ca ii 8542 Å observations (Socas-Navarro 2005; Louis et al. 2021) and in pores using the He i 10830 Å multiplet (Solanki et al. 2003). While Ca ii is partially sensitive to temperatures, the He i line is not, and thus cannot be used to establish a direct link between heating and electric currents in the atmosphere.

Observational evidence for magnetic reconnection in the lower atmosphere comes from the association of small-scale optical or ultraviolet (UV) brightenings, such as Ellerman bombs, UV bursts, and jets near or above patches of opposite magnetic polarity in the photosphere (e.g., Vissers et al. 2013; Chitta et al. 2017; Tiwari et al. 2019; Ortiz et al. 2020), while numerical simulations show how these events could be related to heating in current sheets (e.g, Ni et al. 2015; Danilovic 2017; Hansteen et al. 2019; Syntelis & Priest 2020).

High-resolution observations of the free-free millimeter (mm) continuum are now provided by the Atacama Large Millimeter/sub-millimeter Array (ALMA, Wootten & Thompson 2009). This radiation is optically thick in the chromopshere, and the opacity is dominated by electron-proton collisions (see review by Wedemeyer et al. 2016). The mm continuum provides strong temperature constraints in inversions of non-LTE lines (da Silva Santos et al. 2018, 2020a), which will allow us to revise estimates of radiative energy losses that can be used to benchmark numerical simulations.

Small-scale transient *mm-bursts* in ARs have also been linked to magnetic reconnection events (da Silva Santos et al. 2020b), but the lack of chromospheric magnetic field measurements did not enable a definitive conclusion. Here, we conducted a follow-up study that combines ALMA Band 3 (100 GHz or 3 mm) data with optical spectropolarimetry obtained at the 1-m Swedish Solar Telescope (SST, Scharmer et al. 2003), which provides further evidence for heating in the upper chromosphere in an AR by current dissipation of up to ∼5 kW m^{-2} at the current Band 3 spatial resolution (∼ 1.2″). This is supported by a magnetohydrostatic extrapolation and quantitatively reproduced by a 3-D radiative-magnetohydrodynamics (r-MHD) simulation.

2. Observations

We obtained simultaneous interferometric brightness temperature, T_b, maps of the 3 mm continuum with ALMA and spectropolarimetric observations using the CRISP instrument (Scharmer et al. 2008) at the SST in the Fe I 6173 Å and the Ca II 8542 Å lines (hereafter λ6173 and λ8542) of NOAA AR 12738 on April 13, 2019. We also use ultraviolet (UV) imaging provided by the Atmospheric Imaging Assembly (AIA, Lemen et al. 2012) and magnetogram data from the Helioseismic and Magnetic Imager (HMI, Scherrer et al. 2012) onboard the Solar Dynamics Observatory (SDO, Pesnell et al. 2012).

The ALMA dataset consists of T_b maps taken approximately between 18:20-18:55 UTC and 19:16-19:51 UTC at 2 s cadence with 140 s calibration intervals every 10 min. These data have been previously presented by da Silva Santos et al. (2020b) to which we refer for further details of the data reduction and calibration. In this paper we only use ALMA maps taken within the time span of the SST observations (see below). The field-of-view (FOV) has a diameter of 60″ and the pixel scale is 0.3″. The noise root-mean-square level is approximately 20 K.

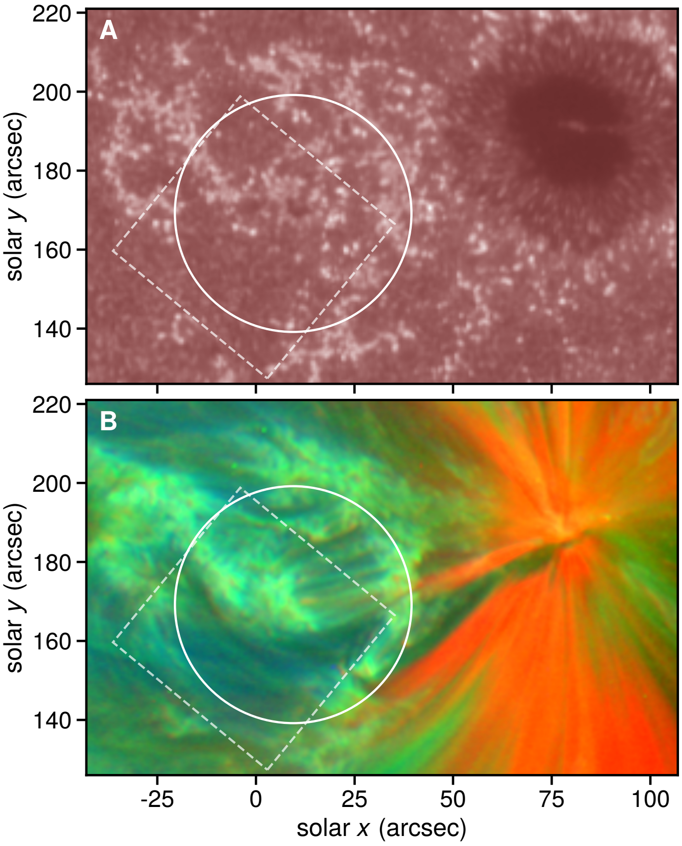

Fig. 1: Extended view of NOAA AR 12738 provided by SDO. *Panel A:* SDO/AIA 1700 Å intensity in square-root scale; *panel B:* composite of AIA 171 Å (red), 193 Å (green), and 211 Å (blue) intensities (unsharpned). The solid circle and dashed square show the ALMA and SST fields, respectively.

Coordination between ALMA in Chile and the SST in La Palma is challenging because of the difference in time zone. The SST/CRISP observations started as soon as the seeing conditions improved in the late afternoon but it was technically unfeasible to prolong the campaign for a long period given the closeness to local sunset. Therefore, the CRISP spectropolarimetric data (full-Stokes) consists of a single line scan of sufficient quality in 17 wavelength positions in λ8542 in the range ±700 mÅ and 15 positions in λ6173 within ±275 mÅ from line center taken between 18:48:36 UTC and 18:48:56 UTC.

The SST data were reduced using the `CRISPRED` pipeline (de la Cruz Rodríguez et al. 2015), which includes flat-field and dark correction, cross-talk correction, polarimetric calibration, image reconstruction through Multi-Object Multi-Frame Blind Deconvolution (MOMFBD, Löfdahl 2002; van Noort et al. 2005), and fringe removal using Fourier filtering. An additional fringe removal step using principal component analysis was necessary in order to remove large-scale patterns in Stokes Q and U (Pietrow et al. 2020). The absolute intensity and wavelength calibrations were performed using the solar atlas of Neckel & Labs (1984) as reference. The pixel scale is 0.059″. We coaligned the CRISP and HMI data by cross-correlating the 6173 Å continuum im-

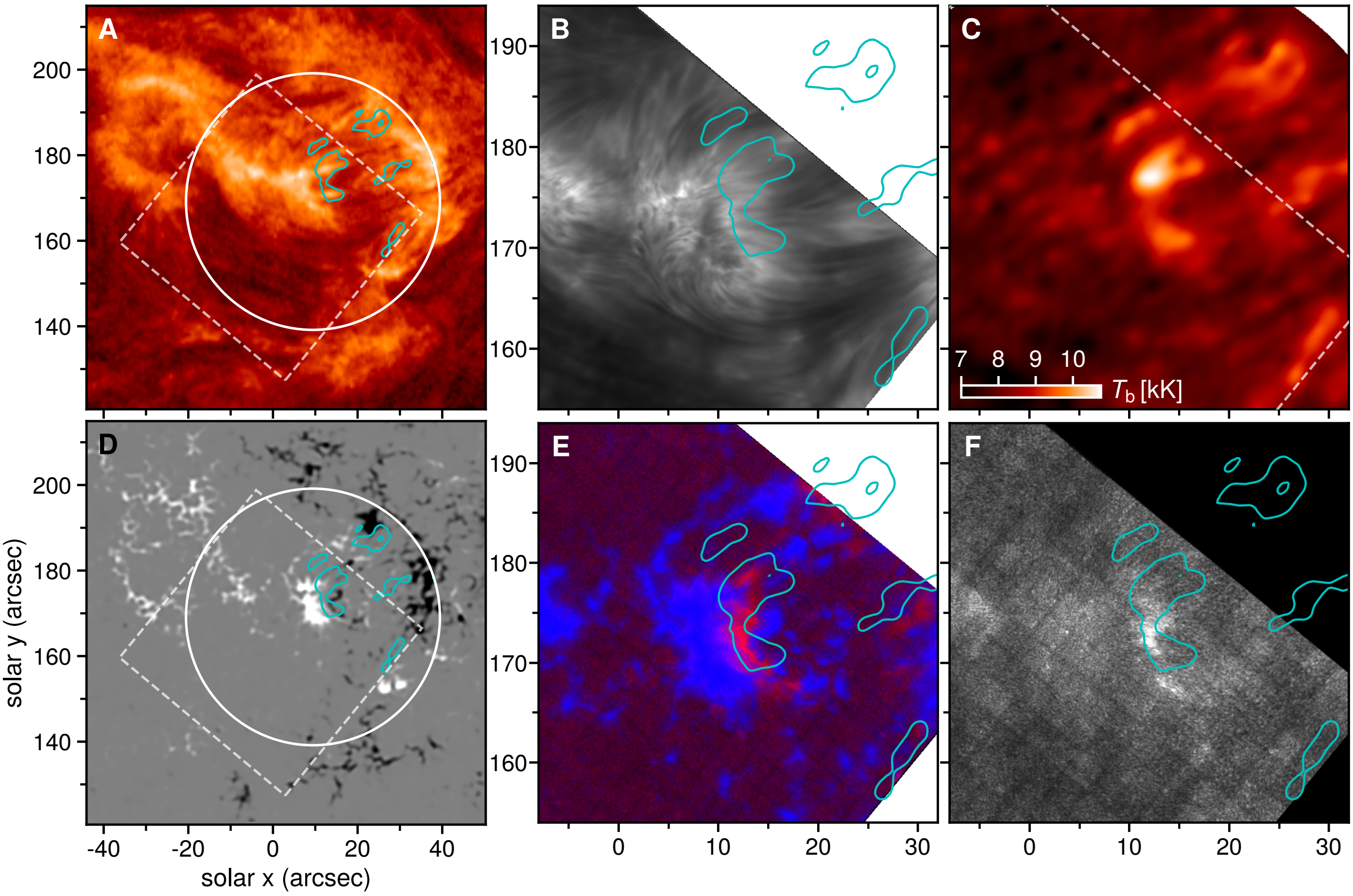

Fig. 2: Multiwavelength imaging of a solar active region. The leftmost panels show an extended view of the target, while the ones on the right show a closer look at the center. *Panel A:* AIA 304 Å intensity in logarithmic scale (18:48:53 UTC); *panel B:* SST/CRISP λ8542 Å core (18:48:41 UTC); *panel C:* ALMA brightness temperature at 3 mm (18:48:53 UTC); *panel D:* HMI LOS magnetogram clipped at +/- 1 kG (white/black, 18:49:30 UTC); *panel E:* composite of total linear polarization (red) and total circular polarization (blue) in λ6173 (18:48:53 UTC); *panel F:* TLP in λ8542 (18:48:41 UTC). The solid circle and dashed square show the ALMA and SST fields. The cyan contours correspond to T_b[3 mm] = 9 kK.

ages taken by both instruments. The calibrated SST and ALMA datasets were analyzed using inversion codes (Section 3.1).

The UV and extreme-UV (EUV) images taken by AIA and the line-of-sight (LOS) magnetograms obtained by HMI were downloaded from the Virtual Solar Observatory using the `vso_search` routine in SolarSoftWare (SSW) (Freeland & Handy 1998); they were further processed using IDL tools in SSW and the `SunPy` package (SunPy Community et al. 2015) as described in da Silva Santos et al. (2020b). The LOS magnetograms were deconvolved using `Enhance`[1] (Díaz Baso & Asensio Ramos 2018). In addition, we used the full-vector magnetogram that was closest in time (taken at 18:48:01 UTC) to the CRISP scans for the magnetic field extrapolation (Section 3.2). The vector magnetogram has been processed with the SHARP pipeline (Bobra et al. 2014) and it was obtained from the JSOC interface [2].

Figure 1 shows a context view of the AR provided by SDO. The SST and ALMA pointings were on a group of pores and an arch-filament system (AFS) southwest of a large sunspot close to disk center. The EUV composite image was generated using the `make_lupton_rgb` function in `Astropy` (Astropy Collaboration et al. 2018; Lupton et al. 2004). The focus of this paper is the area surrounding the pore at the center of the ALMA FOV, which is the location of the Western footpoints of the AFS.

3. Methods

3.1. Data inversions

We run two different inversion codes on the SST data for different purposes: `PyMilne`[3] (de la Cruz Rodríguez 2019) – a code based on the Milne-Eddington (ME) approximation for photospheric lines using analytic response functions (Orozco Suárez & Del Toro Iniesta 2007), and `STiC`[4] (de la Cruz Rodríguez et al. 2019) – a multi-atom, non-LTE inversion code based on the Rybicki-Hummer code (RH, Uitenbroek 2001) that is suitable for both photospheric and chromospheric lines. The former provides the mean magnetic field vector within the formation region of the lines in a large FOV in a quick manner, whereas the latter requires more computing power but it allows for a detailed investigation of the thermodynamic stratification of the plasma

---

[1] https://github.com/cdiazbas/enhance

[2] http://jsoc.stanford.edu/HMI/HARPS.html

[3] https://github.com/jaimedelacruz/pyMilne

[4] https://github.com/jaimedelacruz/stic

as function of logarithmic optical depth of the 500 nm continuum (here simply $\log\tau$), while taking radiative transfer effects into account (e.g., de la Cruz Rodríguez & van Noort 2017).

3.1.1. Milne-Eddington inversions

We fitted the λ6173 spectra taken by SST/CRISP using `PyMilne` in order to provide an input for the magnetic field extrapolation code (Section 3.2). We took into account the spectral point-spread-function of the instrument and cavity errors (de la Cruz Rodríguez et al. 2015). The magnetic filing factor is assumed to be unity. The results are shown in the supplementary Fig. A.2.

Upper limits on the uncertainty in the parameters can be obtained from their spatial variation on scales shorter than those of typical photospheric features (e.g., granule size ∼1″). Using 5×5 px boxes at five different locations in the magnetic areas of the region of interest (ROI; see Fig. 3), we find average standard deviations of $\delta\|B\| = 27$ G, $\delta v_{\rm LOS} = 0.07\,{\rm km\,s^{-1}}$, $\delta\theta = 2°$, and $\delta\phi = 8°$, in the magnetic field strength, line-of-sight velocity, inclination angle, and azimuth angle, respectively.

3.1.2. Non-LTE inversions

We also run non-LTE inversions of the λ6173 and λ8542 lines along with the ALMA $T_{\rm b}$[3 mm] map using the `STiC` code similarly to the approach described in da Silva Santos et al. (2018). The Band 3 $T_{\rm b}$ maps were converted into intensity in c.g.s. units using the Planck function and linearly resampled to the pixel scale of the CRISP data. The inherent inversion uncertainties (see below) outweigh interpolation uncertainties. We note that there is a factor of ten difference in spatial resolution between the optical and mm diagnostics. Multiresolution spectral data can be dealt with using linear operators and global inversion schemes (e.g., de la Cruz Rodríguez 2019) but this has not yet been implemented into `STiC`. Therefore, we have decided to preserve the high-resolution information provided by the SST/CRISP spectropolarimetry and oversample the ALMA maps. This approach worked well here because of the distinct formation heights of λ8542 and the 1.25mm continuum. The high-resolution information in the λ6173 and λ8542 lines provides the temperature stratification at high resolution in the lower atmosphere. Because the chromosphere at depths lower than $\log\tau \sim -5$ is so unconstrained from inversions of those spectral lines (da Silva Santos et al. 2018), `STiC` will essentially provide a low-resolution upper chromosphere constrained by ALMA on top of the high-resolution lower atmosphere constrained by the spectral lines. We restricted the inversions to a ∼16.5″×24.8″ subfield that encloses the ROI in order to reduce the computational cost. This analysis step used a few million core-hours.

We treat each pixel independently (1.5-D approximation) by simultaneously solving the statistical equilibrium equation for non-LTE populations of a 4-level H atom, a 6-level Ca II atom, and a 16-level Fe I atom along with the charge conservation equation, while other atoms and molecules are treated in LTE. Compared to LTE, treating the hydrogen atom in non-LTE and correcting the electron densities using charge conservation provides more realistic values that directly impact the calculation of the opacity in the mm continuum (e.g., da Silva Santos et al. 2020a). We find that treating the Fe I atom in non-LTE leads to average differences in the temperature and magnetic field strength of the order of a few per cent at $\log\tau = 0$ (relative to LTE). Differences in the field strength can be up to ∼ 60% in some patches. Smitha et al. (2020) investigated this in detail for the Fe I 6301, 6302 Å lines using a more complete atomic model, but this would further increase the computational cost of our inversions. This is not critical for our conclusions since we are mainly interested in estimating radiative losses in the chromosphere. However, these effects contribute to the uncertainties of the ME inversions and field extrapolations (Section 3.2). We then run another spectral synthesis solving the statistical equilibrium equation for a 11-level Mg II atom in order to obtain population densities and radiative rates for computing radiative energy losses (Section 3.4). The calculations include PRD in the Mg II h and k lines. The gas pressure is obtained by integration of the hydrostatic equilibrium equation and the value at the top boundary is treated as a free parameter (de la Cruz Rodríguez et al. 2019).

The polarization signals are assumed to be dominated by the Zeeman effect and we do not take the Hanle effect into account. This is a good approximation since the ROI features magnetic fields stronger than 500 G (Centeno et al. 2021).

`STiC` uses parameterization by nodes that are interpolated using Bézier splines in an optical depth grid. We used nine nodes in temperature, four nodes in line-of-sight velocity, and two nodes in microturbulence, parallel and transverse magnetic field, and magnetic azimuth angle.

The uncertainties were estimated using a Monte-Carlo approach (Press et al. 1992) on selected pixels in the ROI (supplementary Fig. A.3). After obtaining good fits to the SST and ALMA observations, we generated up to 100 different synthetic spectra adding a random component that is the sum in quadrature of white noise and flux calibration uncertainties. The latter amounts to less than 1% for the spectral lines (Neckel & Labs 1984) and about 5% for the 3 mm continua. The synthetic spectra were inverted using different randomly generated atmospheres as initial guesses. This provides probability distributions for each parameter from which we computed the 16th, 50th and 84th percentiles at every optical depth (supplementary Fig. A.3). Typical uncertainties in temperature are of the order of ∼50 K or lower within $\log\tau = [-4, 0]$, but they increase at lower optical depths reaching ∼600 K at $\log\tau = -6$ below which the response functions of the diagnostics are weak. The uncertainty in the magnetic field strength is ∼10-20 G for the longitudinal (or LOS) component and ∼10-70 G for the transverse component within $\log\tau = [-5, 0]$. The sensitivity of the λ6173 and λ8542 lines to magnetic fields is weak at optical depths lower than $\log\tau = -5$.

3.2. Magnetic field extrapolation

We performed a magnetic field extrapolation using a magneto-hydrostatic (MHS) model based on the SST and HMI data. Since the SST/CRISP FOV covers only part of the magnetic connectivity, we embedded a cutout of the FOV in the SHARP-processed (disambiguated) HMI vector magnetogram, which covers the entire AR (top panels in supplementary Fig. A.4). This way we make use of the high-resolution information provided by the SST data in the ROI and we take advantage of the more extended HMI FOV for context. This is necessary to interpret the interaction of small- and large-scale loop systems. The resulting magnetogram is in cylindrical-equal-area projection (CEA) coordinates.

To ensure consistency between the CRISP and HMI magnetograms, we disambiguated the azimuth angle provided by the ME inversion of the CRISP data by imposing an acute angle with the HMI/SHARP magnetogram. Both magnetograms are derived from the same spectral line (λ6173). The borders of the CRISP cutout were smoothed with a Gaussian kernel. Finally, the maps of the three components of the magnetic field vector, $\boldsymbol{B}$, were

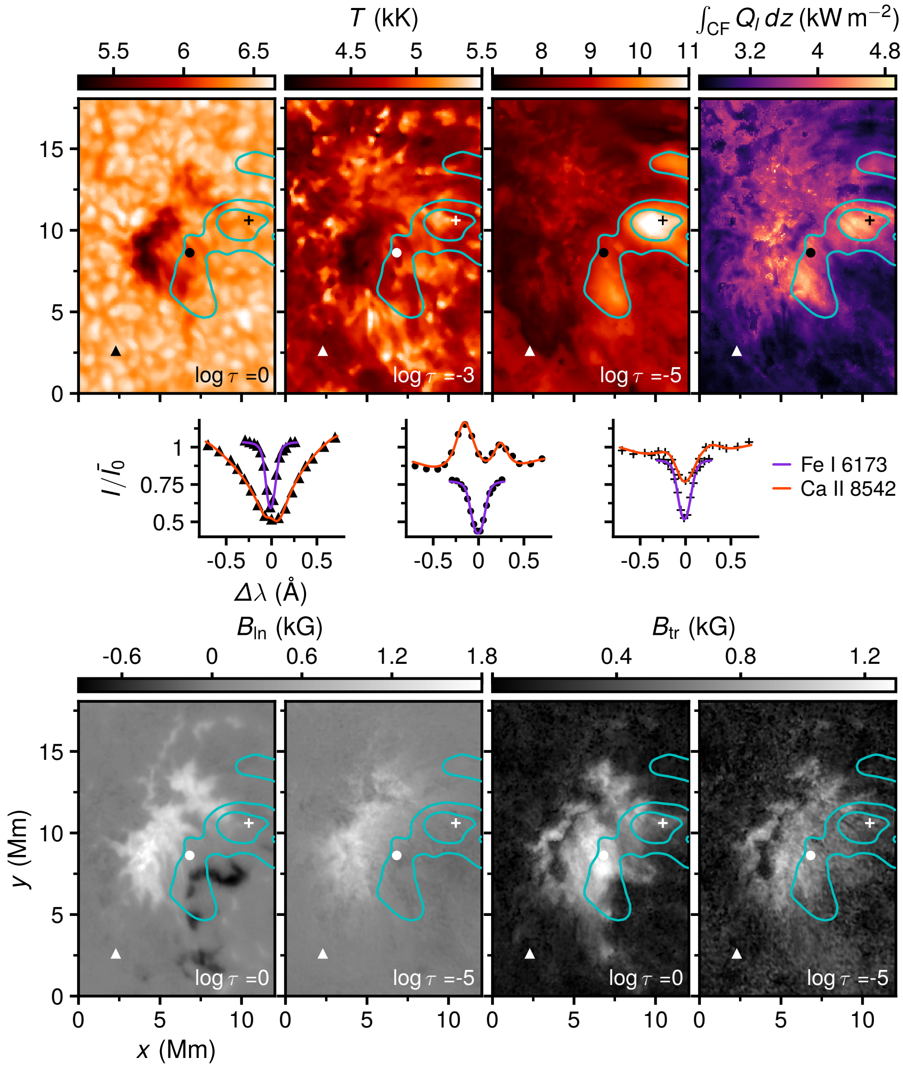

Fig. 3. Non-LTE inversions of the spectral data and radiative losses in the upper chromosphere. Temperature, integrated radiative losses within the contribution function of the 3 mm continuum, longitudinal field strength, and transverse field strength at selected optical depths from the photosphere to the chromosphere. The cyan contours correspond to $T_b[3\,\text{mm}] = 9$ and 10 kK. The middle row shows example observed (markers) and fitted (solid lines) intensity of the λ6173 and λ8542 lines at three locations indicated by different markers overlaid on the other panels; the intensity is normalized by $\bar{I}_0$ – the mean intensity at the bluest sampled wavelength of each line.

convolved with a median filter to reduce the impact of bad pixels and inversion noise in the extrapolation.

The MHS model takes into account the effect of plasma forces which cannot be ignored in the lower atmosphere. An optimization approach is used to numerically solve the equations (Zhu & Wiegelmann 2019):

$$\frac{1}{\mu_0}(\nabla \times \boldsymbol{B}) \times \boldsymbol{B} - \nabla p + \rho\, \boldsymbol{g} = 0, \tag{1}$$

$$\nabla \cdot \boldsymbol{B} = 0, \tag{2}$$

starting from a nonlinear force-free field extrapolation as initial guess (Wiegelmann 2004). Here, μ_0 is the magnetic permeability, p is the gas pressure, ρ is the mass density, and $\boldsymbol{g}$ is the gravitational acceleration. The optimization procedure aims to reach a static equilibrium state between the Lorentz force, the pressure gradient, and gravity.

The model uses the photospheric vector magnetogram (Section 3.1.1) as the lower boundary condition. The plasma pressure at the lower boundary is calculated from

$$p + \frac{B_z^2}{2} = P_{\text{ph}}, \tag{3}$$

where P_{ph}, is a typical photospheric pressure. Further details of the MHS method can be found in Zhu & Wiegelmann (2018); Zhu et al. (2020). The resulting model has a size of 2000×1800×256 pixels with a uniform pixel scale of 40 km.

3.3. 3-D radiative-magnetohydrodynamics simulation

The simulation presented here was performed with the `MURaM` code (Vögler et al. 2005; Rempel 2017), which includes the following physics: single fluid MHD, 3-D grey LTE radiative transfer, a tabulated LTE equation of state, Spitzer heat conduction, and optically thin radiative losses in the corona based on `CHIANTI` (Landi et al. 2012). The chromospheric and coronal parts of the simulation domain is heated by the Poynting flux generated through magnetoconvection in the photosphere and convection zone. Earlier simulations with this code have reproduced many observed chromospheric phenomena (e.g., Bjørgen et al. 2019; Leenaarts 2020).

The simulation domain has an extent of 40 × 40 × 22 Mm, spanning in the vertical direction from −8 Mm to 14 Mm above the average $\tau_{500\,\text{nm}} = 1$ height. The pixel size is 0.078 Mm. The run was initialized with a bipolar uniform magnetic field of 200 G (Cameron et al. 2011), which is added to the well-developed nonmagnetic convection simulation to form extended magnetic field concentrations at meso- to super-granular scales. This was done with the aim of reproducing the plasma dynamics of solar plage – regions of moderate magnetic activity. The computational domain was then extended to include the upper solar atmosphere, and the magnetic field from the preexisting simulation was used for potential field extrapolation into the rest of the domain. The new simulation was then run until a relaxed state was achieved. An additional bipolar flux system was advected through the bottom boundary through an ellipsoidal region with major axes (a, b) = (3, 1) Mm and field strength of 8000 G (Cheung et al. 2019), which emerged from the convection zone into the chromosphere directly beneath the preexisting filaments. Once the flux reaches the photosphere, its field strength decreased to around 1.5 kG.

Since the non-LTE spectral synthesis is quite computationally intensive and memory-demanding, here we analyzed one single simulation snapshot where we identified a region of enhanced $T_\mathrm{b}[3\,\mathrm{mm}]$ at a later stage of the flux emergence $t = 17$ min after the magnetic flux reached the photosphere. Anyhow, the lack of spectropolarimetric time series in λ6173 and λ8542 does not allow us to compare the observations and the unraveling of the simulated flux emergence.

We computed the emerging intensities in λ8542 from the simulation in non-LTE 1.5-D (full-Stokes) using `STiC` and in 3-D (intensity only) using `Multi3D` (Leenaarts & Carlsson 2009). The synthetic Ca II lines were convolved with the CRISP response function. The 3 mm continuum intensities were computed assuming statistical equilibrium and charge conservation using `STiC` (see also da Silva Santos et al. 2020a). Besides the synthetic intensities we also stored the opacities $\alpha(\nu, z)$ as function of frequency ν and height z for each pixel. We investigated the formation of the 3 mm continuum in detail using contribution functions (CF) defined as

$$\mathrm{CF}_\nu(z) = \alpha_\nu(z)\, S_\nu(z)\, e^{-\tau_\nu(z)}, \tag{4}$$

where $\nu = 100$ GHz, S_ν is the source function, which is given by the Planck function, and τ_ν is the optical depth. This quantity essentially quantifies the contribution from different heights of the atmosphere to the emerging intensities.

3.4. Radiative energy losses

Besides the radiative losses, Q_l, that can be directly retrieved from the `MURaM` simulation output (Rempel 2017), we also obtained Q_l[STiC] from the non-LTE synthesis with `STiC` by summing the contributions to the radiative cooling from the Ca II H, K, infrared triplet, Mg II h, k, UV triplet, Hα, and Lyα lines as follows

$$Q_\mathrm{l}[\mathrm{STiC}] = h\nu_0(n_\mathrm{u}R_\mathrm{ul} - n_\mathrm{l}R_\mathrm{lu}), \tag{5}$$

where h is the Planck constant, ν_0 is the frequency of the transition, n_u and n_l are the population densities of the upper and lower levels, and R_ul and R_lu are the radiative rates of the transitions (e.g., Díaz Baso et al. 2021). These chromospheric losses are more suitable for comparison with the losses that can be inferred from observations using data inversions (Section 3.1.2).

Total radiative losses were obtained by integration in the height range spanned by the CF of the 3 mm continuum using a threshold of 1% of the maximum in each pixel. This criterion was used both for the CFs obtained from the simulation and observations.

4. Results

AR 12738 showed ongoing magnetic flux emergence into a preexisting AFS. The ALMA map (Fig. 2C) reveals elongated patches of enhanced $T_\mathrm{b}[3\,\mathrm{mm}]$ by ~3,000 K relative to QS values, which is indicative of local heating in the upper chromosphere. The ALMA time series (supplementary movie) shows recurring brightenings exhibiting several hundred kelvin $T_\mathrm{b}[3\,\mathrm{mm}]$ variations, which last from a few tens of seconds to a few minutes with no clear periodicity. These hot spots are also well-visible in the AIA 304 Å images (Fig. 2A) and partially in AIA 171 Å (Fig. 1) but not in hotter channels. Correlation between Band 3 brightenings and coronal emission in ARs has been reported before (da Silva Santos et al. 2020b; Brajša et al. 2021). There are other bright regions in the FOV in the 304 Å images that have no counterpart in the ALMA maps. This may imply varying relative differences in formation heights of both diagnostics at different locations.

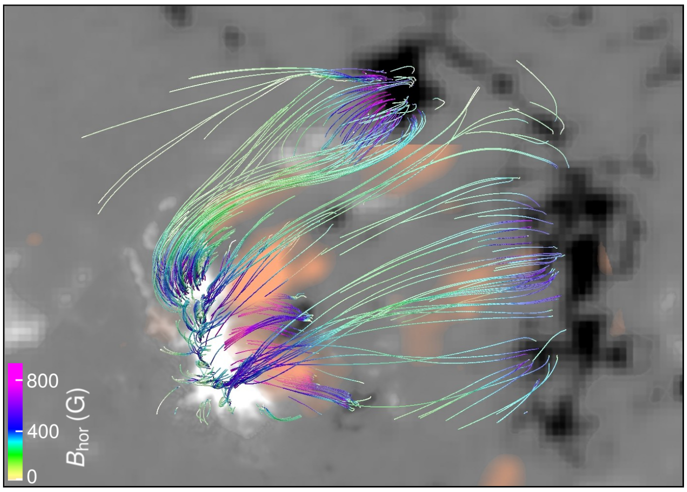

Fig. 4: Magnetohydrostatic extrapolation of the SST and HMI composite magnetogram and millimeter continuum brightness. The background shows a SST/CRISP and HMI magnetogram composite image clipped at +/-1 kG (white/black). The magnetic field lines are computed from the MHS extrapolation and they are color-coded with the horizontal field strength. The pink shade show regions where T_b [3 mm] > 9 kK.

Comparison to the HMI LOS magnetogram (Fig. 2D) shows that this region is located between concentrations of magnetic field of opposite polarity, which are the footpoints of chromospheric loops that connect the two patches. The SST data indeed shows short bright loop-like structure in the λ8542 core (Fig. 2B) and significant total linear polarization signals (TLP = $\int \sqrt{Q^2 + U^2}/I\, d\lambda$) indicative of strong transverse magnetic field in the photosphere and chromosphere (Figs. 2E, 2F). The composite image of other AIA EUV channels shows longer dark filaments overlying the small-scale loops (Fig. 1).

4.1. Physical properties from inversions

The non-LTE inversions provide a well-resolved temperature structure from the photosphere to the top of the chromosphere where the 3 mm continuum is formed. The sensitivity of the spectra to magnetic fields is lower, and the inversions provide the vector magnetic field in the photosphere and mid-chromosphere.

Figure 3 shows the results of the `STiC` inversions. We find increased temperatures in the chromosphere at least up to optical depth $\log\tau \sim -6$ where $T \sim 10{,}000$ K, which is of the order of the observed T_b [3 mm]. The warm locations feature λ8542 profiles with central reversals or raised intensities in the wings and small Doppler shifts ($\lesssim 4\,\mathrm{km\,s^{-1}}$), which are well-reproduced by our models (supplementary Fig. A.3).

We computed the radiative energy losses as a proxy for the heating rate, which cannot be directly observed. In Fig. 3 we

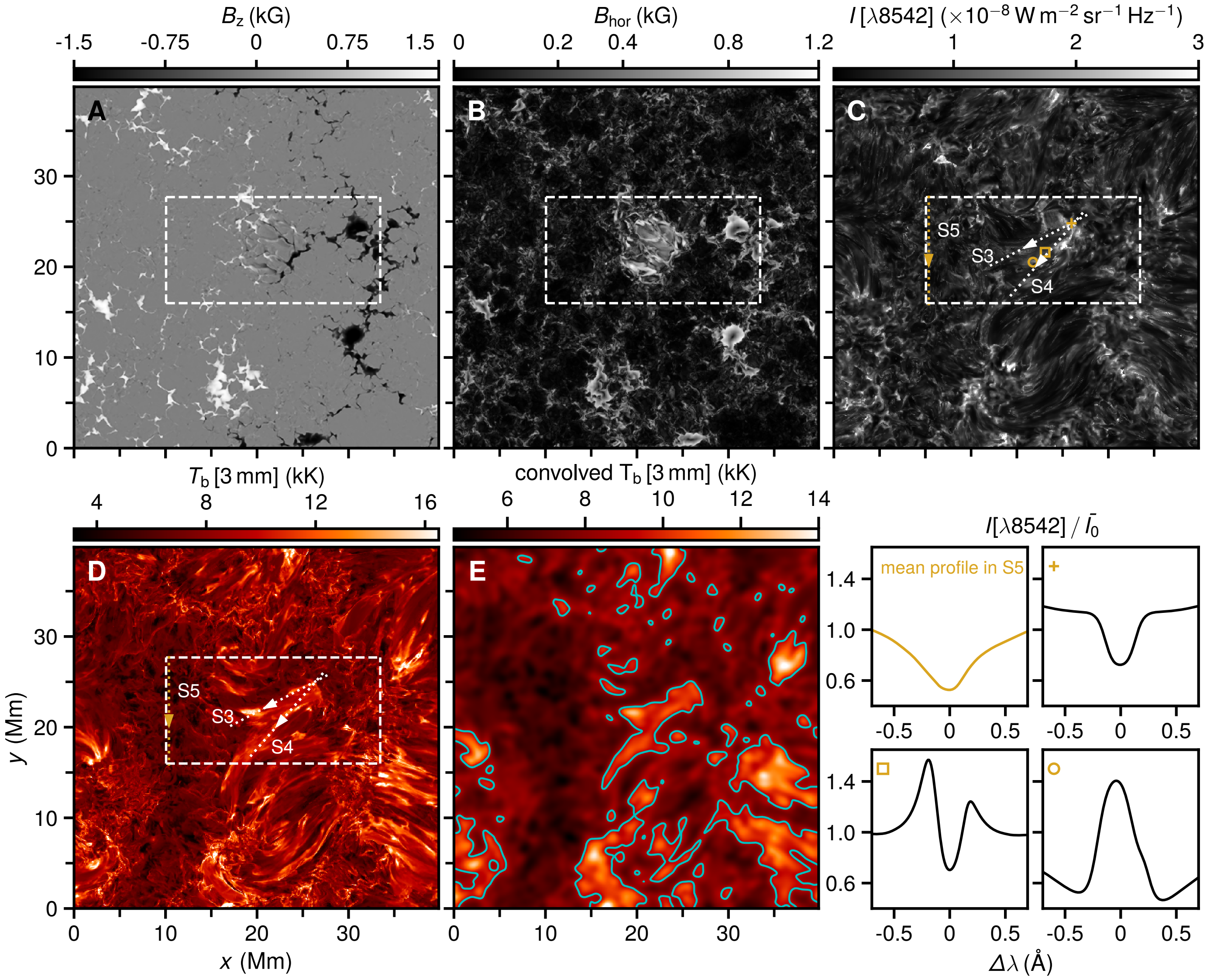

Fig. 5: Simulated magnetograms and synthetic emission. Strength of the vertical (*panel A*) and horizontal (*panel B*) components of the magnetic field at $z = 0$ Mm; *panel B* has been gamma-adjusted for display purposes. *Panel C:* intensity in the core of λ8542; the range is capped for display purposes. *Panel D* and *panel E*: continuum T_b[3 mm] at full resolution and convolved with a Gaussian kernel with full-width-at-half-maximum of 1.2″; the cyan contours show T_b[3 mm] = 9 kK. The dashed box delimits the area displayed in Fig. 6B, 6C. The lower right panels show selected λ8542 profiles (normalized intensity) in the flux emergence region. Vertical cuts through various parameters of the simulated atmosphere along the slices *S3*, *S4*, and *S5* are displayed in the supplementary Fig. A.6.

also show integrated losses from the inferred atmosphere in the strongest lines of H I, Ca II, and Mg II (Section 3.4) in the height range spanned by the CF of the 3 mm continuum. This is done in geometrical height scale assuming hydrostatic equilibrium. Energy losses range from 2.6 to 4.9 kW m^{-2} with a mean value of ~4 kW m^{-2} within the T_b [3 mm] = 9 kK contours, which is higher than previous estimates of ~2 kW m^{-2} in the upper chromosphere (Withbroe & Noyes 1977).

The longitudinal and transverse photospheric field in the ROI have a maximum strength of $|B_{\rm ln}| = 1890$ G and $|B_{\rm tr}| = 1380$ G and the uncertainty is of the order of 10 G. The chromospheric magnetic field is overall weaker, but the transverse component remains strong with an average (maximum) value of $|B_{\rm tr}| \sim 480$ G (1060 G) with an uncertainty of ~70 G at $\log\tau = -5$ within the T_b [3 mm] = 9 kK contours. The transverse field traces the near-horizontal tops of the emerging loops and coincides with higher temperature regions.

4.2. The magnetic topology

The fidelity of the magnetic field derived from the inversions is high, but the vertical resolution is low and the FOV is small. Therefore, we complement our analysis with a MHS extrapolation based on a high-resolution magnetogram derived from the SST λ6173 data (supplementary Fig. A.2) embedded in a lower resolution magnetogram provided by HMI (Section 3.2).

Figure 4 was produced using the `VAPOR` software[5] (Shaomeng et al. 2019), and it shows a 3-D rendering of the

---

[5] `www.vapor.ucar.edu`

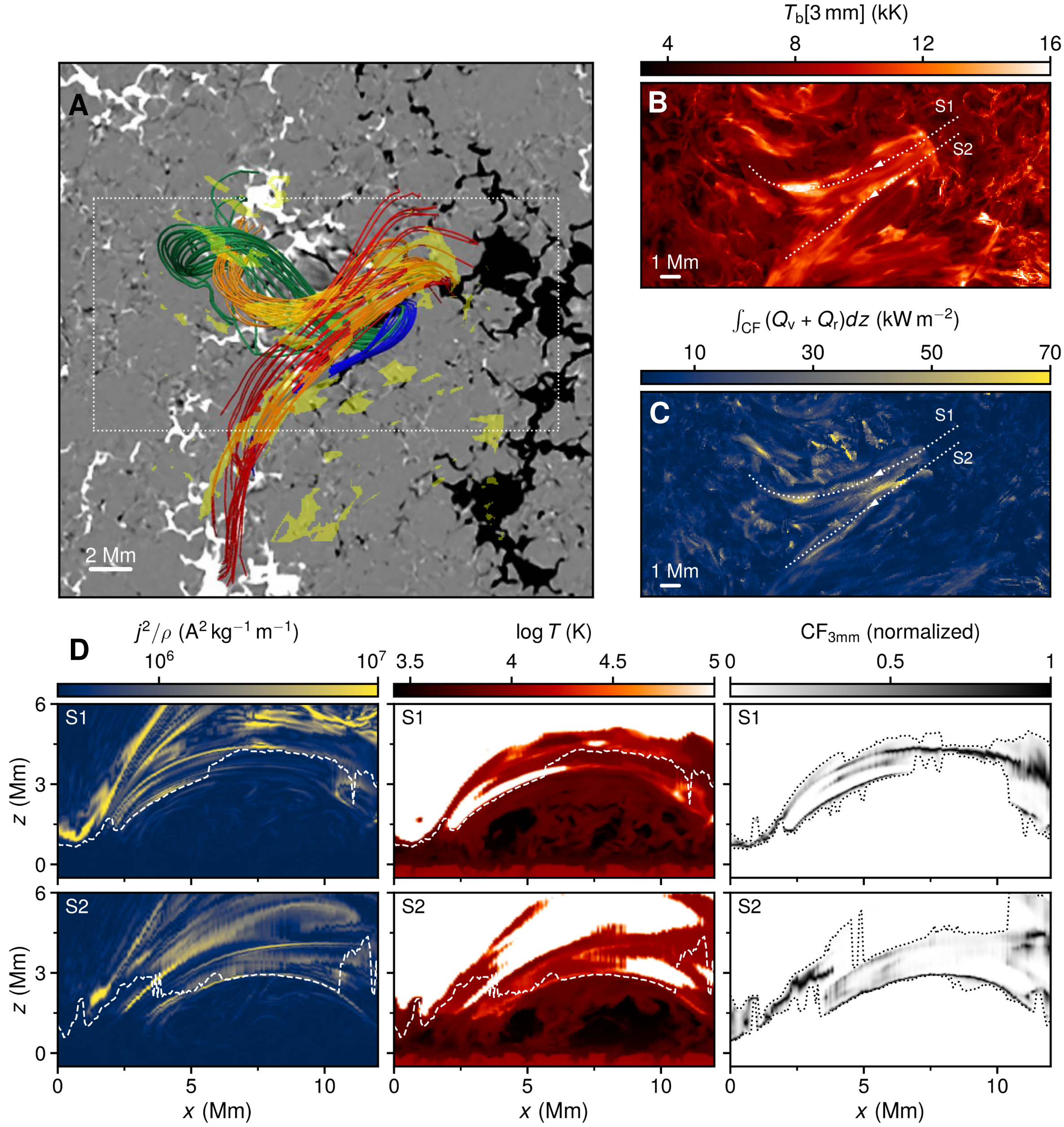

Fig. 6: Magnetic topology, heating rates, and the formation of the millimeter continuum in a 3-D radiative-magnetohydrodynamics simulation. *Panel A:* photospheric magnetogram clipped at +/- 1 kG; the yellow shade shows where T_b[3mm] > 9 kK. The area inside the dotted box is displayed in *panels B* and *C*, which show T_b[3mm] and the sum of viscous and resistive heating integrated within the CF of the 3 mm continuum. The group of *panels D* show from the left to the right: current density squared per mass unit (square-root scaling), logarithm of temperature, and CF$_{3\,\mathrm{mm}}$ slices along the dotted paths *S1* and *S2* overlaid on *panels B* and *C*; the white dashed lines show where $\tau_{3\,\mathrm{mm}} = 1$, and the dotted black lines show where CF is at 1% of the maximum in each column.

overlying field connecting the pore and the plage region, whose direction is the same as the AFS in the EUV images (c.f. Fig. 1).

Comparison with Fig. 2B confirms that the field lines align with the direction of the bright λ8542 fibrils inside the ALMA T_b contours, in agreement with the picture drawn from the imaging and inversions. The horizontal magnetic field strength in the short loops derived from the extrapolation (as high as ~ 800 G around $z \sim 1$ Mm) is consistent with the inversion results. Patches of high T_b [3 mm] coincide with the interaction region between the loop systems where current sheets (tangential discontinuities) must exist between them.

We computed the current density ($\boldsymbol{j} = \nabla \times \boldsymbol{B}/\mu_0$) from the extrapolation for completeness (supplementary Fig. A.4), but we note that spurious currents arise from the lack of smoothness in the magnetic field introduced by inversion noise in the magnetograms and the azimuth angle disambiguation, as well as limitations of the MHS extrapolation algorithm itself (Zhu & Wiegelmann 2018). We find current strands over a range of heights relevant to the formation of the 3 mm continuum (~1-4 Mm, Fig. 6 and Fig. 7C) cospatial with both the short λ8542 loops and the long, overlying ones seen in the AIA images, but we could not identify a single height that correlates strongly with T_b[3 mm]. However, we do expect spatial/temporal variations of the formation height of the mm continuum (e.g., Loukitcheva et al. 2015; Martínez-Sykora et al. 2020).

We attempted to correlate T_b[3 mm] with j^2/ρ in the MHS extrapolation at the height where $\tau_{3\,\mathrm{mm}} = 1$ obtained from the non-LTE inversions assuming hydrostatic equilibrium (typically $z \sim 1.5$-1.8 Mm) and taking into account the fact that the zero point of the MHS extrapolation is defined by the mean formation height of λ6173, but this turned out to be inconclusive. This comparison was also made in column mass scale. This is partly due to the fact that the height scales obtained from these two methods are different, but we also expect the MHS extrapolation to underestimate the magnetic structure and field strength compared to λ8542 spectropolarimetry (Vissers et al. 2021), so the electric current values have some uncertainty. Moreover, the height-integration effect of the CF of the 3 mm continuum may smear such correlation as further discussed in Section 4.3.

Therefore, we cannot unambiguously link the observed millimeter emission to heating in current sheets based on these data alone. Nonetheless, the 3 mm continuum forms above λ8542 (da Silva Santos et al. 2018), but below the He II 304 Å line, which strongly suggests that the mm continuum originates in the the shear layer.

4.3. Investigating the formation of the mm continuum

To gain further insight into the magnetic flux emergence and how electric currents heat the atmosphere in that process, we ran a 3-D r-MHD simulation using `MURaM` as explained in Section 3.3. Figure 5 displays the strength of the vertical and horizontal components of the photospheric magnetic field vector along with the synthetic emission in the core of λ8542 (corrected for Doppler shifts) and T_b[3 mm]. In order to simulate the effect of the ALMA beam to first order, we convolved T_b[3 mm] at the simulation resolution (Fig. 5D) with a Gaussian kernel with full-width-at-half-maximum FWHM = 1.2″ (Fig. 5E). In this paper we are primarily interested in the region inside the dashed box that encloses a patch of emerging flux and where we see some compact mm brightenings as well as bright fibrils. At the ALMA resolution the bright strands appear more blob-like as in the observations (Fig. 2C). The simulation is also able to reproduce λ8542 profiles qualitatively similar to the observations featuring central reversals and raised intensities in the wings. There are patches where the line core is in full emission, which we do not find in the single CRISP scan that we have. Emission profiles are uncommon in the simulation, and they occur at sites of enhanced heating at the $\tau = 1$ layer of the line core (e.g., *panels S4* in Fig. 8). We would need a longer λ8542 time series to investigate whether this kind of emission profiles can occur as in the simulation.

Figure 6A shows the footprint of the emerging bubble together with field lines highlighting the direction of the emerging loops (green), the overlying filaments (red), and the two sets of reconnected field lines (blue and orange). The synthetic 3 mm emission shows a bifurcated structure following the reconnected field lines in the interaction region (Fig. 6B).

We find enhanced total heating rates, defined as the sum of the viscous, Q_v, and resistive, Q_r, heating within CF$_{3\,\mathrm{mm}}$ in thin strands in the interaction region (Fig. 6C). The mean (maximum) values at the location where T_b [3 mm] $> 10{,}000$ K are 12 kW m^{-2} (184 kW m^{-2}). This heating is caused by dissipation of currents and viscous dissipation of mass flows, both of which are driven by the interaction of the magnetic loop systems. This does not only directly cause Joule heating, but also drives flows through the Lorentz force that dissipate through viscosity. Our simulation employs numerical diffusive and resistive terms with an effective magnetic Prandtl number $P_m > 1$ so that viscous heating is the largest contributor. However, in the real chromosphere $P_m < 1$ and the heating is dominated by electric resistivity. The 3 mm continuum is optically thick where $P_m < 1$ (supplementary Fig. A.5).

The vertical cuts along the slices *S1* and *S2* (Fig. 6D) underscore that CF$_{3\,\mathrm{mm}}$ peaks at locations of high j^2/ρ in the chromosphere where there are magnetic field gradients, but the resulting T_b [3 mm] may reflect contributions from multiple strands along the LOS. In supplementary Fig. A.6 we also provide additional 2-D slices of the total heating rates per mass unit, which show the same qualitative picture. The CF$_{3\,\mathrm{mm}}$ shows a loop-like structure following the shape of the chromosphere-transition region boundary where the gas is still partially ionized. Locations of larger j^2/ρ at transition region and coronal temperatures have negligible 3 mm opacity so they do not contribute to T_b [3 mm]. However, the heating rate in those strands can be very large, and hot pockets embedded in the 3 mm formation height range lead to the large peak values in Fig. 6C.

The simulated chromosphere is pervaded by multiple current sheets at different heights and shows a complicated thermal structure (Figs. 6D), while the analysis of the opacity data shows that the formation height of the 3 mm continuum varies significantly across the flux emergence region (Fig. 7C). The CF of the 3 mm continuum peaks where the loop systems meet an angle (Fig. 7B) and the atmosphere is locally heated (see also supplementary Fig. A.6). Figure 7A shows integrated j^2/ρ weighted by CF$_{3\,\mathrm{mm}}$, which reveals the filamentary structure of the heating – very similar to the synthetic emission itself (c.f. Fig. 5D).

The layer where optical depth is unity in the core of λ8542 is typically located below that of the 3 mm continuum in the flux emergence region (supplemtary Fig. A.6). This suggests that the former traces the top of the low-lying fibrils, whereas the latter sees the heating at or above the λ8542 canopy.

Figure 8 shows a comparison between the total radiative losses Q_l and Q_l[STiC] in the simulated chromosphere. At the native resolution of the simulation, the losses show the same bifurcated structure in the interaction region (c.f. Fig. 6B, 6C). Total Q_l in the simulation reach above 100 kW m^{-2} in some pixels due to the inclusion of losses at transition-region and coronal temperatures in thin pockets within the formation range of the millimeter continuum (c.f. supplementary Fig. A.6). These are not included in the `STiC` losses, hence the lower values. Much of the filamentary structure is lost at the ALMA resolution, and the values of the radiative losses decrease significantly; the mean(standard deviation) is $\sim 6(\pm 2)$ kW m^{-2} where T_b [3 mm] > 9 kK, which is similar to the values derived from the non-LTE inversions of the SST and ALMA data (Fig. 3).

5. Discussion and conclusions

In this paper we present an analysis of joint SST and ALMA observations of an AR on the Sun using inversion methods, field extrapolations, and a numerical simulation. We find enhanced T_b[3 mm] and bright λ8542 profiles between a pore and parasitic opposite polarity patch in the photosphere. This is also the location of short, low-lying chromospheric fibrils, where the magnetic field is more horizontal to the solar surface, underneath an overlying AFS seen in absorption in the AIA EUV channels.

Our analysis validates dissipation in current sheets as, at least, a locally dominant source of atmospheric heating, which produces brightenings in chromospheric diagnostics within ARs. Integrated radiative losses in the strongest chromospheric lines

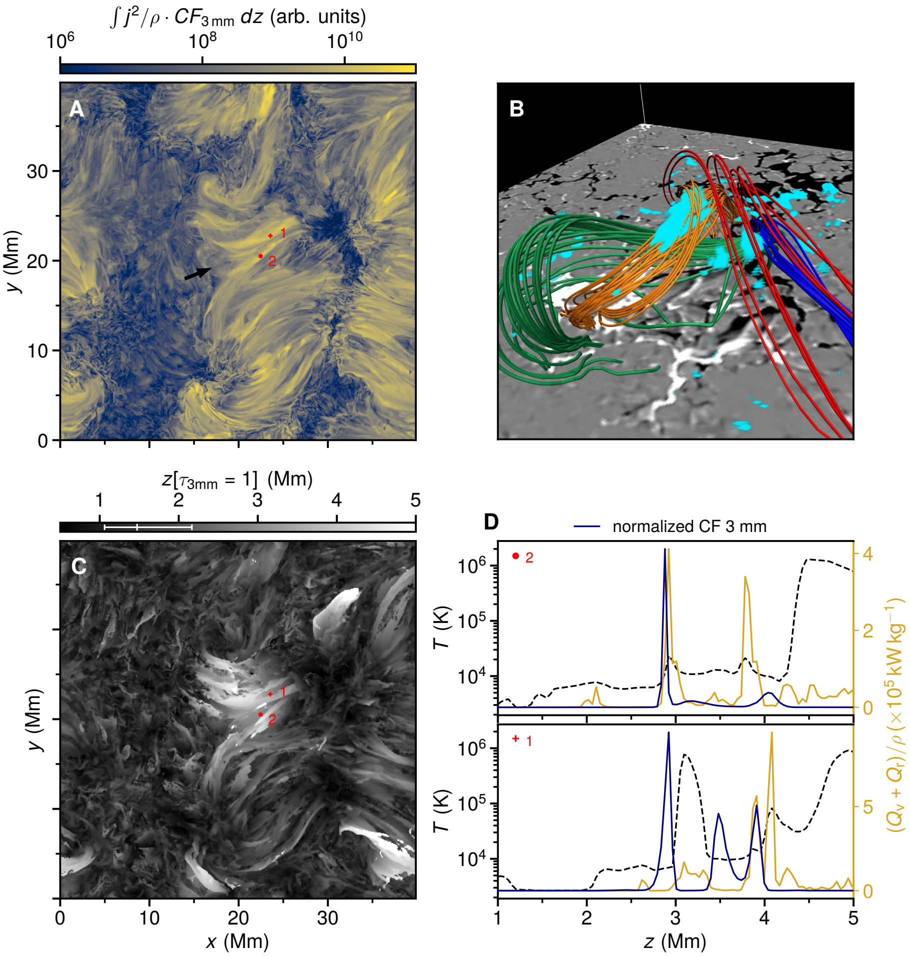

Fig. 7. Heating rates and the formation of the millimeter continuum in the simulation. *Panel A:* integrated j^2/ρ weighted by the contribution function of the 3 mm continuum ($\mathrm{CF}_{3\,\mathrm{mm}}$). *Panel B:* photospheric magnetogram (range ±1 kG) with 3-D rendering of magnetic field lines and $\mathrm{CF}_{3\,\mathrm{mm}}$ (blue shade) of the region indicated by the arrow in *panel A*; a threshold has been applied to the CF values not to hide the field lines. *Panel C:* Height at which $\tau = 1$ at 3 mm; the errorbar overlaid on the colormap shows the median and the range between the 16th and 84th percentiles of the distribution. *Panel D:* temperature (dashed lines), total heating rates per mass (yellow lines), and $\mathrm{CF}_{3\,\mathrm{mm}}$ (blue lines) as function of height at two locations indicated in *panels A* and *C*.

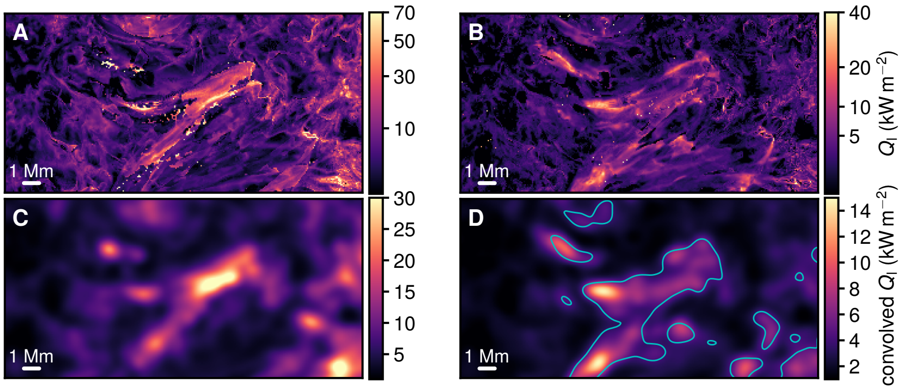

Fig. 8. Radiative losses in the simulation. Total radiative losses integrated within $\mathrm{CF}_{3\mathrm{mm}}$ from the `MURaM` output (*panel A*) and non-LTE values calculated using `STiC` (*panel B*) at full resolution; *panels C* and *D* show the corresponding quantities convolved with a Gaussian kernel with FWHM of 1.2″ . The cyan contours show $T_b[3\,\mathrm{mm}] = 9\,\mathrm{kK}$. The top row panels are displayed in square-root scale.

obtained from the simulation can be an order of magnitude higher than the ones determined from the observations. However, degrading the former to the spatial resolution of ALMA yields a mean(standard deviation) value of $\sim 6\,(\pm 2)\,\mathrm{kW\,m^{-2}}$, which is consistent with the observed values. The heating occurs on spatial scales that are not resolved in the ALMA Band 3 data. We note that this is only an approximate way of comparing losses obtained from observations and simulations at different spatial resolutions. In principle we would need to investigate the impact of the lack of constraints in the inversions on the estimates of the radiative losses by inverting synthetic data from the simulation at different resolutions, but this is beyond the scope of this paper.

Our estimates are much lower than the values reported in a observed magnetic reconnection event of up to $\sim 160\,\mathrm{kW\,m^{-2}}$ (Díaz Baso et al. 2021). This is partly due to differences in the integration method, but most importantly that event was much stronger and showed strong flows and an associated surge, which we did not detect. However, our limited spectropolarimetric data only provides one time frame and does not allow us to investigate dynamics in detail. The ALMA time series does show recurring elongated brightenings at that location prior to the SST campaign, which would be consistent with the bright strands that we see in the simulation.

We note that the simulation makes use of numerical diffusivity and viscosity terms that are larger than their physical values. This is common in numerical simulations of the type employed here, and experiments show that this has only a marginal effect on the total energy dissipation rate (Galsgaard & Nordlund 1996; Rempel 2017), which is mainly determined by the Poynting flux input in the photosphere. The simulation was run with an effective numerical magnetic Prandtl number $P_\mathrm{m} > 1$; about two thirds of the energy dissipated in the chromosphere is through viscosity and one third by electric resistivity. The chromosphere has a P_m that is significantly below unity, especially if ambipolar diffusion is taken into account (Martínez-Sykora et al. 2012), which appears as an additional cross-field resistivity in the MHD approximation. While the majority of the dissipation of magnetic energy in the simulated chromosphere occurs through the Lorentz force, which drives flows that are then damped through viscosity, the solar chromosphere dissipates the majority of the energy through currents (e.g., Rempel 2017; Brandenburg & Rempel 2019).

Although our simulation lacks some chromospheric physics such as ion-neutral interactions and non-equilibrium ionization (e.g., Khomenko & Collados 2012; Nóbrega-Siverio et al. 2020), it reproduces remarkably well the observed magnetic configuration, optical and radio spectra, and energetics. It also shows how the flux emergence leads to enhanced emission in the mm continuum, which is a good proxy for local chromospheric heating, and how the opacity may vary across the flux emergence region. However, the height-integration effect of the contribution function implies that the observed brightness temperatures may be a weighted average of contributions from several different layers along the LOS (see also Martínez-Sykora et al. 2020), which complicates the interpretation of observations.

The MHS extrapolation reveals a textbook magnetic topology similar to previously proposed models of the interaction of emergent flux and the canopy (e.g., Solanki et al. 2003; Cheung & Isobe 2014; Ortiz et al. 2016), leading to the formation of current sheets between the two flux systems (e.g., Galsgaard et al. 2007; Archontis & Hansteen 2014). If the loop interaction occurs at coronal heights this may lead to much higher temperatures ($\gtrsim 1$ MK) and produce the recently discovered *campfire* EUV signatures as simulations suggest (Chen et al. 2021).

These findings may play a role in explaining the solar cycle modulation of brightness temperatures in the millimeter range and their correlation with sunspot number (Giménez de Castro et al. 2020), as well as the excess millimeter brightness in chromospheres of other stars (MacGregor et al. 2015; Liseau et al. 2015; O'Gorman et al. 2017). Our analysis quantifies radiative losses, which can also be used to benchmark simulations of solar and stellar atmospheres.

Acknowledgements. This paper makes use of the following ALMA data: ADS/JAO.ALMA#2018.1.01518.S. The Swedish 1-m Solar Telescope is operated on the island of La Palma by the Institute for Solar Physics of Stockholm University in the Spanish Observatorio del Roque de los Muchachos of the Instituto de Astrofísica de Canarias. The Institute for Solar Physics is supported by a grant for research infrastructures of national importance from the Swedish Research Council (registration number 2017-00625). ALMA is a partnership of ESO (representing its member states), NSF (USA) and NINS (Japan), together with NRC (Canada), MOST and ASIAA (Taiwan), and KASI (Republic of Korea), in cooperation with the Republic of Chile. The Joint ALMA Observatory is operated by ESO, AUI/NRAO and NAOJ. Part of the calculations were performed on resources provided by the Swedish National Infrastructure for Computing (SNIC) at the National Supercomputer Centre (NSC) at Linköping University and the PDC Centre for High Performance Computing (PDC-HPC) at the Royal Institute of Technology in Stockholm. This project has received funding from the European Research Council (ERC) under the European Union's Horizon 2020 research and innovation program (SUNMAG grant agreement 759548 and SOLARNET grant agreement 824135), the Knut and Alice Wallenberg Foundation, Swedish Research Council (2021-05613) and Swedish National Space Agency (2021-00116); this material is partly based upon work supported by the National Center for Atmospheric Research, which is a major facility sponsored by the National Science Foundation under Cooperative Agreement No. 1852977; X.Z. is supported by the mobility program (M-0068) of the Sino-German Science Center. This research has made use of `Astropy` (`https://astropy.org`) – a community-developed core Python package for Astronomy (Astropy Collaboration et al. 2018) and `SunPy` (`https://sunpy.org`) – an open-source and free community-developed solar data analysis Python package (SunPy Community et al. 2015).

References

Abbasvand, V., Sobotka, M., Švanda, M., et al. 2020, A&A, 642, A52
Archontis, V. & Hansteen, V. 2014, ApJ, 788, L2
Astropy Collaboration, Price-Whelan, A. M., Sipőcz, B. M., et al. 2018, Astron. J, 156, 123
Barczynski, K., Peter, H., Chitta, L. P., & Solanki, S. K. 2018, A&A, 619, A5
Bjørgen, J. P., Leenaarts, J., Rempel, M., et al. 2019, Astron. Astrophys, 631, A33
Bobra, M. G., Sun, X., Hoeksema, J. T., et al. 2014, Sol. Phys., 289, 3549
Brajša, R., Skokić, I., Sudar, D., et al. 2021, A&A, 651, A6
Brandenburg, A. & Rempel, M. 2019, Astrophys. J., 879, 57
Cameron, R., Vögler, A., & Schüssler, M. 2011, Astron. Astrophys, 533, A86
Carlsson, M., De Pontieu, B., & Hansteen, V. H. 2019, ARA&A, 57, 189
Centeno, R., de la Cruz Rodríguez, J., & del Pino Alemán, T. 2021, ApJ, 918, 15
Chen, Y., Przybylski, D., Peter, H., et al. 2021, A&A, 656, L7
Cheung, M. C. M. & Isobe, H. 2014, Living Rev. Sol. Phys., 11, 3
Cheung, M. C. M., Rempel, M., Chintzoglou, G., et al. 2019, Nature Astronomy, 3, 160
Chitta, L. P., Peter, H., Young, P. R., & Huang, Y. M. 2017, A&A, 605, A49
Cirtain, J. W., Golub, L., Winebarger, A. R., et al. 2013, Nature, 493, 501
da Silva Santos, J. M., de la Cruz Rodríguez, J., & Leenaarts, J. 2018, Astron. Astrophys, 620, A124
da Silva Santos, J. M., de la Cruz Rodríguez, J., Leenaarts, J., et al. 2020a, Astron. Astrophys, 634, A56
da Silva Santos, J. M., de la Cruz Rodríguez, J., White, S. M., et al. 2020b, Astron. Astrophys, 643, A41
Danilovic, S. 2017, A&A, 601, A122
de la Cruz Rodríguez, J. 2019, Astron. Astrophys, 631, A153
de la Cruz Rodríguez, J., Leenaarts, J., Danilovic, S., & Uitenbroek, H. 2019, Astron. Astrophys, 623, A74
de la Cruz Rodríguez, J., Löfdahl, M. G., Sütterlin, P., Hillberg, T., & Rouppe van der Voort, L. 2015, Astron. Astrophys, 573, A40
de la Cruz Rodríguez, J. & van Noort, M. 2017, Space Sci. Rev., 210, 109
Díaz Baso, C. J. & Asensio Ramos, A. 2018, Astron. Astrophys, 614, A5
Díaz Baso, C. J., de la Cruz Rodríguez, J., & Leenaarts, J. 2021, Astron. Astrophys, 647, A188
Freeland, S. L. & Handy, B. N. 1998, Sol. Phys., 182, 497
Galsgaard, K., Archontis, V., Moreno-Insertis, F., & Hood, A. W. 2007, Astrophys. J., 666, 516
Galsgaard, K. & Nordlund, Å. 1996, J. Geophys. Res., 101, 13445
Giménez de Castro, C. G., Pereira, A. L. G., Valle Silva, J. F., et al. 2020, Astrophys. J., 902, 136
Hansteen, V., Guerreiro, N., De Pontieu, B., & Carlsson, M. 2015, Astrophys. J., 811, 106
Hansteen, V., Ortiz, A., Archontis, V., et al. 2019, A&A, 626, A33
Harvey, K. L. & White, O. R. 1999, ApJ, 515, 812
Khomenko, E. & Collados, M. 2012, ApJ, 747, 87
Klimchuk, J. A. 2015, Philosophical Transactions of the Royal Society of London Series A, 373, 20140256
Landi, E., Del Zanna, G., Young, P. R., Dere, K. P., & Mason, H. E. 2012, ApJ, 744, 99
Leenaarts, J. 2020, Living Reviews in Solar Physics, 17, 3
Leenaarts, J. & Carlsson, M. 2009, in Astronomical Society of the Pacific Conference Series, Vol. 415, The Second Hinode Science Meeting: Beyond Discovery-Toward Understanding, ed. B. Lites, M. Cheung, T. Magara, J. Mariska, & K. Reeves, 87
Leenaarts, J., de la Cruz Rodríguez, J., Danilovic, S., Scharmer, G., & Carlsson, M. 2018, Astron. Astrophys, 612, A28
Lemen, J. R., Title, A. M., Akin, D. J., et al. 2012, Sol. Phys., 275, 17
Lindsey, C. A. & Jefferies, J. T. 1991, ApJ, 383, 443
Liseau, R., Vlemmings, W., Bayo, A., et al. 2015, Astron. Astrophys, 573, L4
Löfdahl, M. G. 2002, in SPIE Conference Series, Vol. 4792, Image Reconstruction from Incomplete Data, ed. P. J. Bones, M. A. Fiddy, & R. P. Millane, 146–155
Louis, R. E., Prasad, A., Beck, C., Choudhary, D. P., & Yalim, M. S. 2021, Astron. Astrophys, 652, L4
Loukitcheva, M., Solanki, S. K., Carlsson, M., & White, S. M. 2015, A&A, 575, A15
Loukitcheva, M., Solanki, S. K., & White, S. M. 2009, Astron. Astrophys, 497, 273
Lupton, R., Blanton, M. R., Fekete, G., et al. 2004, PASP, 116, 133
MacGregor, M. A., Wilner, D. J., Andrews, S. M., Lestrade, J.-F., & Maddison, S. 2015, ApJ, 809, 47

Martínez-Sykora, J., De Pontieu, B., de la Cruz Rodriguez, J., & Chintzoglou, G. 2020, Astrophys. J. Lett., 891, L8

Martínez-Sykora, J., De Pontieu, B., & Hansteen, V. 2012, Astrophys. J., 753, 161

McIntosh, S. W., de Pontieu, B., Carlsson, M., et al. 2011, Nature, 475, 477

Molnar, M. E., Reardon, K. P., Cranmer, S. R., et al. 2021, ApJ, 920, 125

Neckel, H. & Labs, D. 1984, Sol. Phys., 90, 205

Ni, L., Kliem, B., Lin, J., & Wu, N. 2015, ApJ, 799, 79

Nóbrega-Siverio, D., Moreno-Insertis, F., Martínez-Sykora, J., Carlsson, M., & Szydlarski, M. 2020, A&A, 633, A66

O'Gorman, E., Kervella, P., Harper, G. M., et al. 2017, Astron. Astrophys, 602, L10

Orozco Suárez, D. & Del Toro Iniesta, J. C. 2007, Astron. Astrophys, 462, 1137

Ortiz, A., Hansteen, V. H., Bellot Rubio, L. R., et al. 2016, Astrophys. J., 825, 93

Ortiz, A., Hansteen, V. H., Nóbrega-Siverio, D., & Rouppe van der Voort, L. 2020, A&A, 633, A58

Parker, E. N. 1988, Astrophys. J., 330, 474

Pesnell, W. D., Thompson, B. J., & Chamberlin, P. C. 2012, Sol. Phys., 275, 3

Pietrow, A. G. M., Kiselman, D., de la Cruz Rodríguez, J., et al. 2020, Astron. Astrophys, 644, A43

Press, W. H., Teukolsky, S. A., Vetterling, W. T., & Flannery, B. P. 1992, Numerical recipes in C. The art of scientific computing (Cambridge University Press)

Rempel, M. 2017, Astrophys. J., 834, 10

Scharmer, G. B., Bjelksjo, K., Korhonen, T. K., Lindberg, B., & Petterson, B. 2003, in SPIE Conference Series, Vol. 4853, Innovative Telescopes and Instrumentation for Solar Astrophysics, ed. S. L. Keil & S. V. Avakyan, 341–350

Scharmer, G. B., Narayan, G., Hillberg, T., et al. 2008, Astrophys. J. Lett., 689, L69

Scherrer, P. H., Schou, J., Bush, R. I., et al. 2012, Sol. Phys., 275, 207

Schrijver, C. J. 1987, A&A, 180, 241

Shaomeng, L., Stanislaw, J., Scott, P., Leigh, O., & John, C. 2019, Atmosphere, 10

Smitha, H. N., Holzreuter, R., van Noort, M., & Solanki, S. K. 2020, A&A, 633, A157

Socas-Navarro, H. 2005, ApJ, 633, L57

Solanki, S. K., Lagg, A., Woch, J., Krupp, N., & Collados, M. 2003, Nature, 425, 692

SunPy Community, T., Mumford, S. J., Christe, S., et al. 2015, Comput. Sci. Discov., 8, 014009

Syntelis, P. & Priest, E. R. 2020, ApJ, 891, 52

Tiwari, S. K., Panesar, N. K., Moore, R. L., et al. 2019, ApJ, 887, 56

Uitenbroek, H. 2001, Astrophys. J., 557, 389

Van Doorsselaere, T., Srivastava, A. K., Antolin, P., et al. 2020, Space Science Reviews, 216, 140

van Noort, M., Rouppe van der Voort, L., & Löfdahl, M. G. 2005, Sol. Phys., 228, 191

Vissers, G. J. M., Danilovic, S., Zhu, X., et al. 2021, arXiv e-prints, arXiv:2109.02943

Vissers, G. J. M., Rouppe van der Voort, L. H. M., & Rutten, R. J. 2013, ApJ, 774, 32

Vögler, A., Shelyag, S., Schüssler, M., et al. 2005, A&A, 429, 335

Wedemeyer, S., Bastian, T., Brajša, R., et al. 2016, Space Sci. Rev., 200, 1

Wiegelmann, T. 2004, Sol. Phys., 219, 87

Withbroe, G. L. & Noyes, R. W. 1977, ARA&A, 15, 363

Wootten, A. & Thompson, A. R. 2009, IEEE Proceedings, 97, 1463

Zhu, X. & Wiegelmann, T. 2018, Astrophys. J., 866, 130

Zhu, X. & Wiegelmann, T. 2019, Astron. Astrophys, 631, A162

Zhu, X., Wiegelmann, T., & Solanki, S. K. 2020, A&A, 640, A103

Appendix A: Supplementary figures

Figure A.1 displays additional SST/CRISP context data, which clearly shows the pore, surrounding plage, and overlying chromospheric fibrilar structures. Enhanced millimeter brightness (e.g., red contours) generally corresponds to the brightest regions of the $\lambda 8542$ filtergrams.

Figure A.2 shows the results of the ME inversion of the CRISP data. Residual fringe patterns in the Stokes V signals that could not be removed by either Fourier filtering or PCA leave a noticeable imprint on the inclination angle map, but mostly towards the NW and SE sides of the CRISP FOV. The fringing is not seen in the ROI and does not affect the results. The displayed azimuth angle map is not disambiguated but it is fairly smooth between the two opposite polarity patches. The LOS velocities show $\leq 1\,\mathrm{km\,s^{-1}}$ upflows between the opposite photospheric polarities.

Figure A.3 shows the results of the Monte-Carlo `STiC` inversions on three selected pixels in the ROI. The spread in the physical parameters can be used to assess the uncertainties of the inverted models.

Figure A.4 shows the photospheric composite vector magnetogram, which results from the combination of the SST and HMI data, along with the current densities at different heights calculated from the MHS extrapolation for qualitative comparison with the Band 3 brightness contours. The range of heights was chosen based on the insight provided by the simulation.

Figure A.5 shows the magnetic Prandtl number – the ratio of viscosity to the magnetic diffusivity, along 2-D cuts through the simulated atmosphere (c.f. Fig. A.6). Both $\lambda 8542$ and the 3 mm continuum are formed in the low P_m regime.

Figure A.6 displays two vertical cuts through the flux emergence region (*S3* and *S4*) and a cut through a part of the simulation with open field (*S5*) for comparison. The formation height of the 3 mm continuum follows layers of strong radiative cooling. The Joule heating proxy j^2/ρ shows elongated current sheets, which are reflected in the heating terms ($Q_\mathrm{v} + Q_\mathrm{r}$). The radiative cooling Q_l shows roughly the same structure, confirming our use of the radiative losses as a proxy for the heating. The quantity Q_l[STIC] is lower, because it only contains contributions from chromospheric lines.

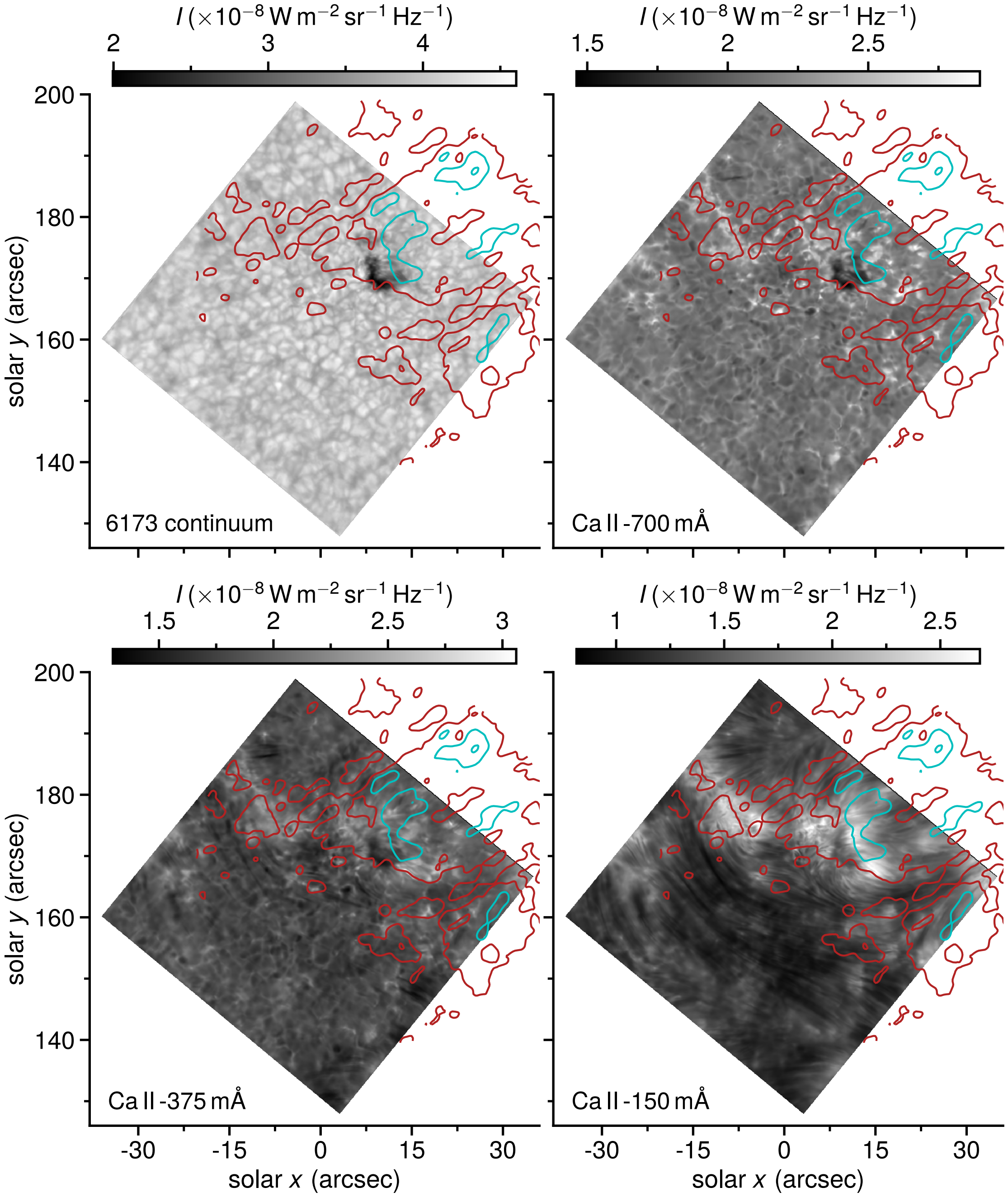

Fig. A.1: SST/CRISP photospheric and chromospheric filtergrams. Intensity in the continuum at 6173 Å and at different wavelengths in the blue wing of λ8542. The red and cyan contours correspond toT_b[3 mm] = 8 and 9 kK mapped by ALMA.

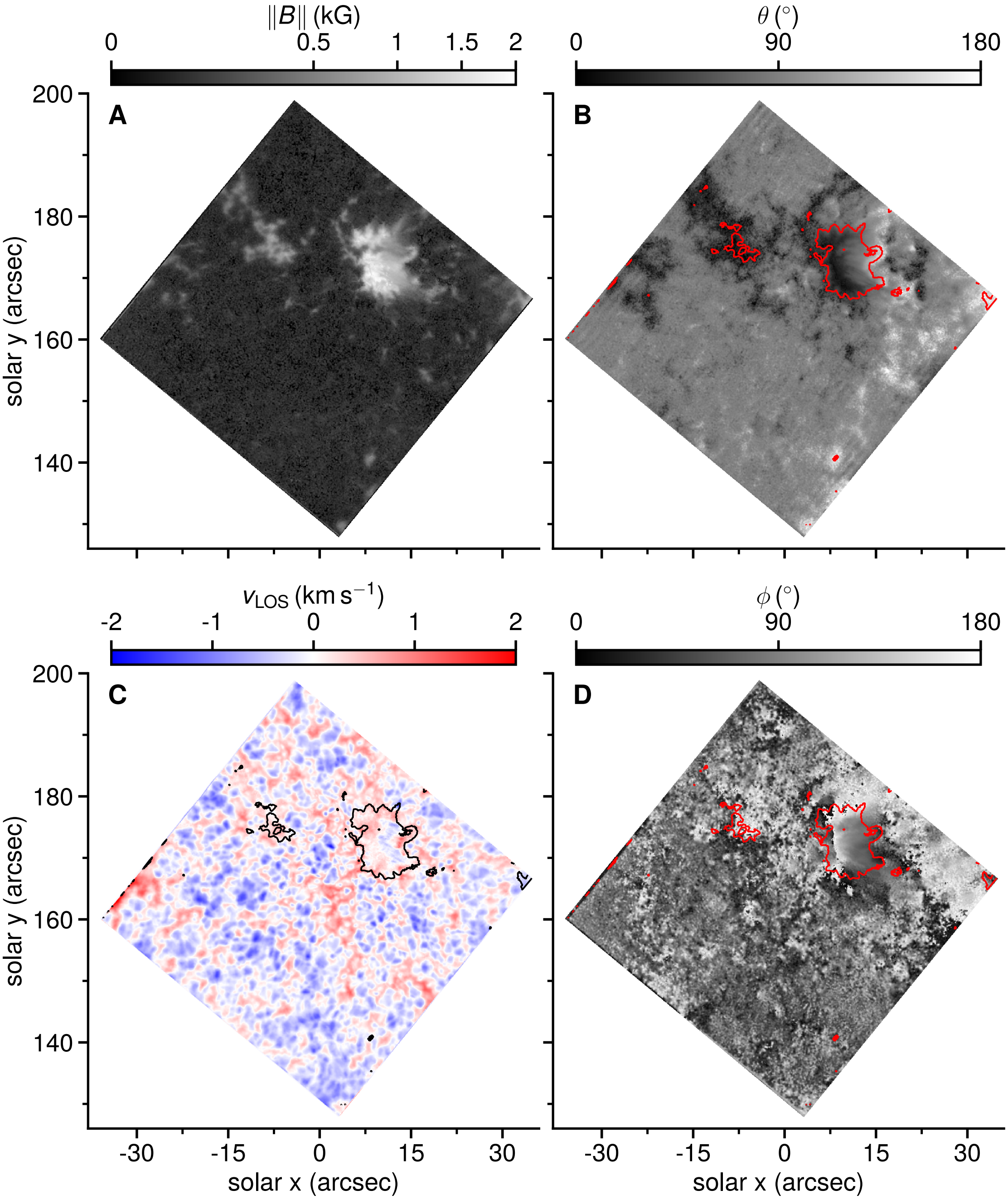

Fig. A.2: Milne-Eddington inversion of the SST/CRISP spectropolarimetry in $\lambda 6173$. *Panel A:* magnetic field strength with square-root colormap scaling; *panel B:* inclination angle; *panel C:* line-of-sight velocity; *panel D:* azimuth angle. The contours correspond to $\|B\| = 0.5\,$kG.

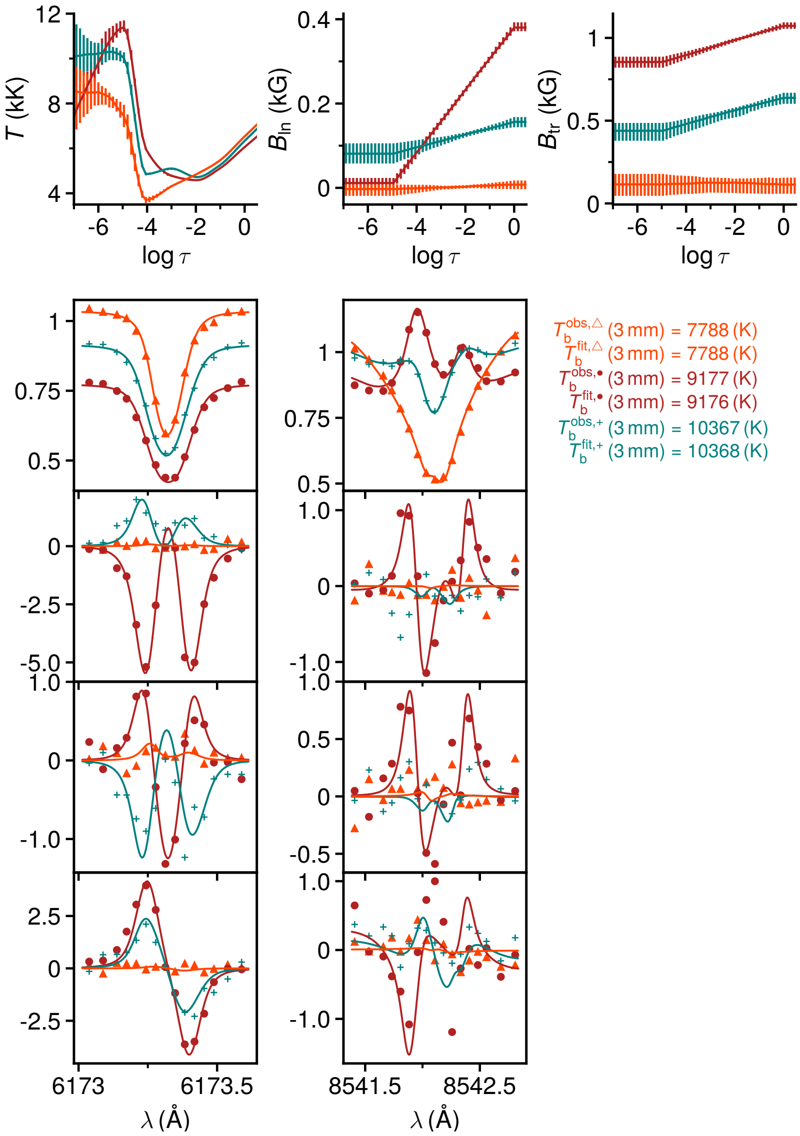

Fig. A.3: Observed and best-fit Stokes profiles and corresponding non-LTE models. The three example profiles (normalized by $\bar{I}_0$ – the mean intensity in the *quiet* part of the FOV at the bluest wavelength) correspond to the markers shown in Fig. 3. Observed and synthetic T_b [3 mm] values are indicated on the right. The solid lines and vertical bars in the top panels show the median and the range between the 16th and 84th percentiles of the Monte-Carlo distributions at each optical depth grid point.

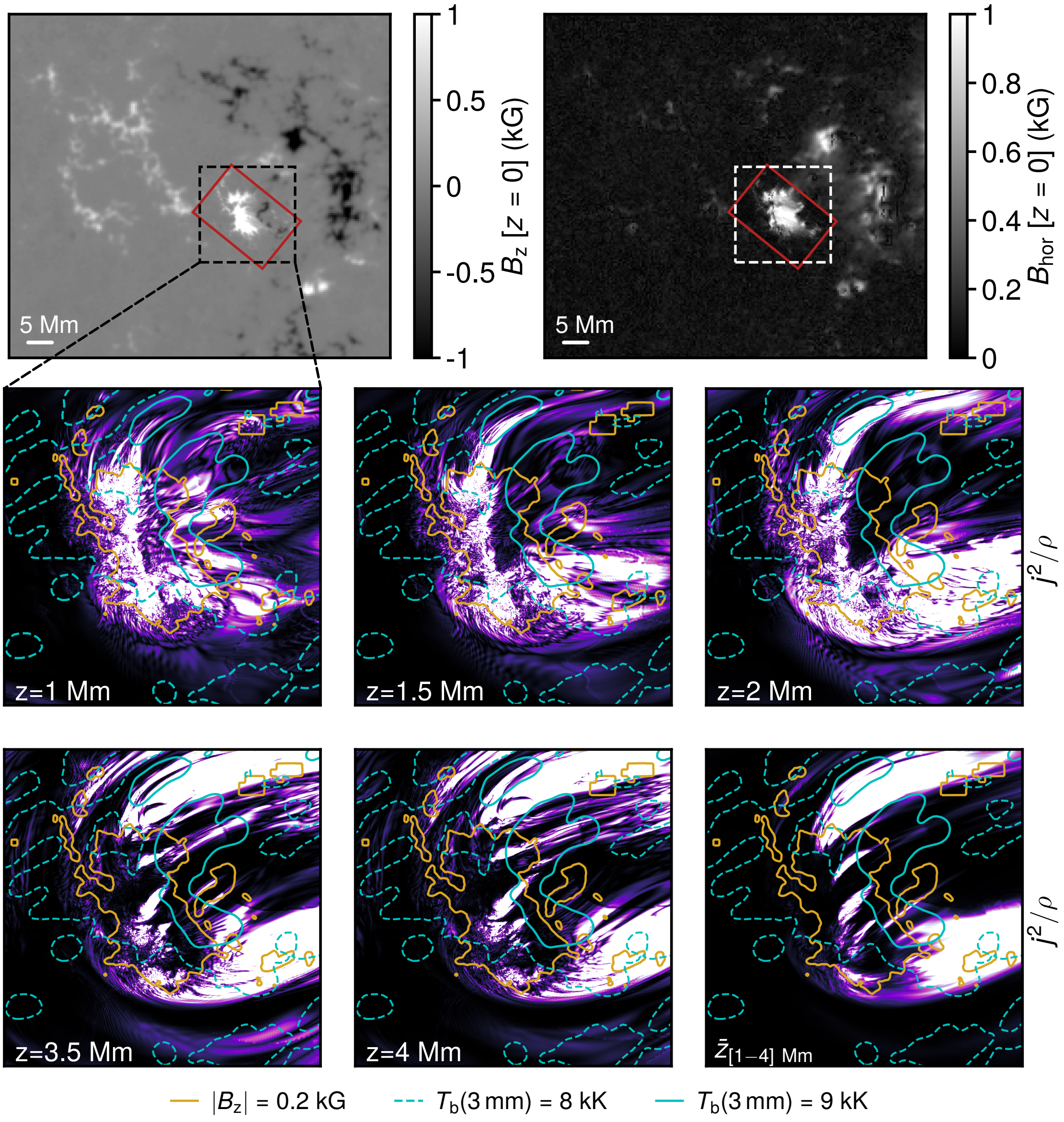

Fig. A.4: Current density calculated from the magnetic field extrapolation. The red rectangle in the top panels delimits the embedded SST/CRISP FOV in the extended HMI magnetogram. The middle and lower rows show j^2/ρ at different heights in square-root scaling and arbitrary units for qualitative comparison with ALMA T_b contour overlays (cyan lines) within the region delimited by the dashed box. The lower right panel shows j^2/ρ averaged over height between $z = [1, 4]$ Mm. The yellow contour indicates $|B_z|$ at $z = 0$ Mm.

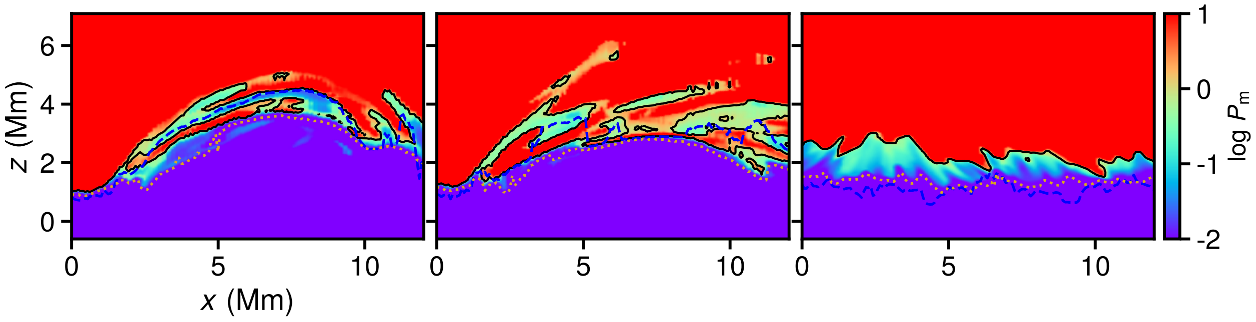

Fig. A.5: Magnetic Prandtl Number. Magnetic Prandtl number in the vertical cuts *S3*, *S4*, and *S5* (see Supplementary Fig. 10). The dashed line shows the $\tau = 1$ layer of the 3 mm continuum, the dotted line the same quantity for the core of λ8542. The solid black line shows $P_m = 1$. The colormap range is capped for display purposes.

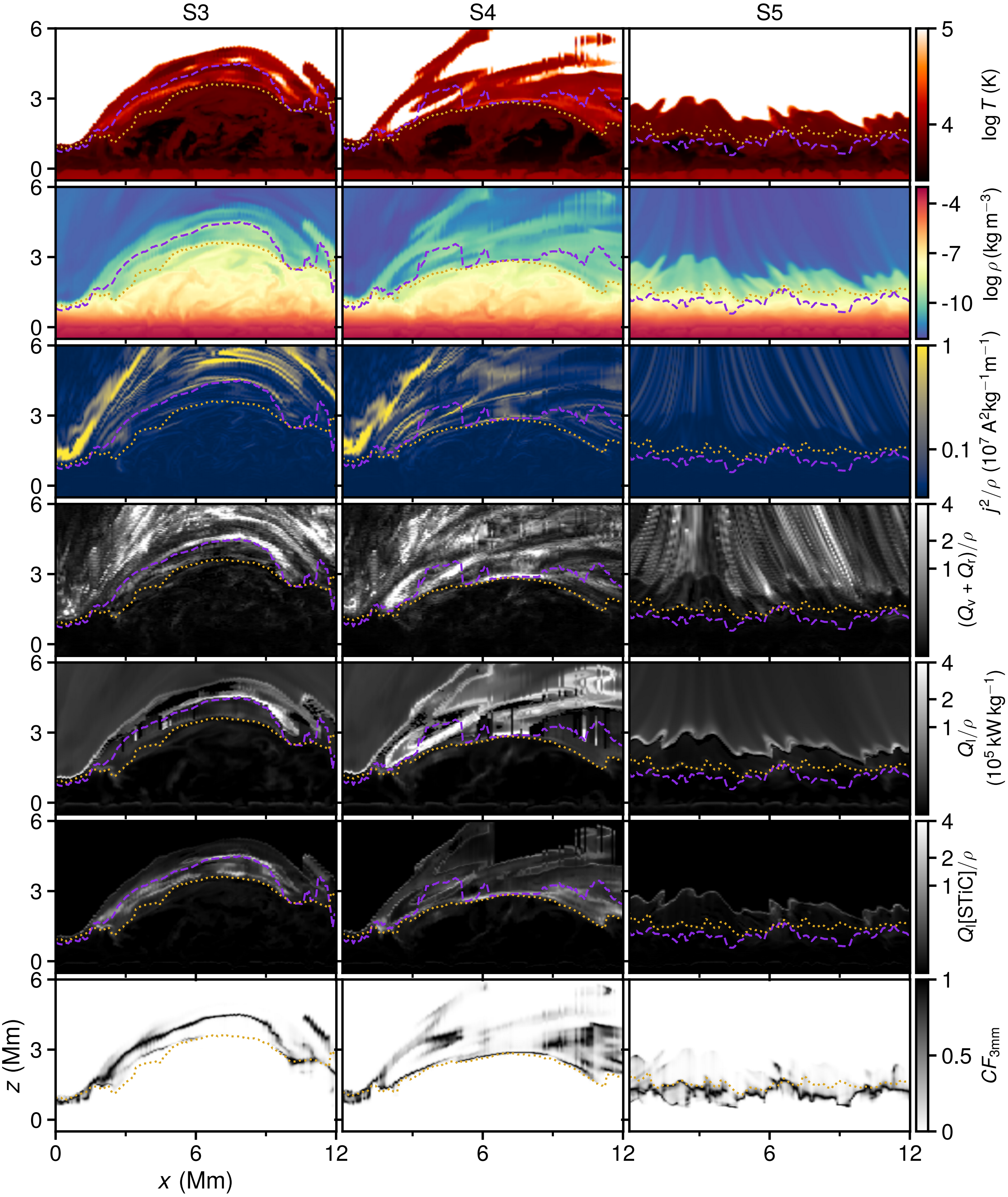

Fig. A.6: Two-dimensional view of the simulation. Vertical cuts through the atmosphere along the slices *S3*, *S4*, and *S5* (see Fig. 5). The dashed line shows the $\tau = 1$ layer of the 3 mm continuum, the dotted line the same quantity for the core of λ8542. With the exception of the two top rows, all panels are displayed in power-law scale.